ChemPubSoc Europe

DOI: 10.1002/cctc.201500380

CHEMCATCHEM Full Papers

AEM 3

Surface Segregation of Fe in Pt–Fe Alloy Nanoparticles: Its Precedence and Effect on the Ordered-Phase Evolution during Thermal Annealing

Sagar Prabhudev,[a] Matthieu Bugnet,[a, b] Guo-Zhen Zhu,[c] Christina Bock,[d] and Gianluigi A. Botton*[a, b]

Coupling electron microscopy techniques with in situ heating ability allows us to study phase transformations on the single-nanoparticle level. We exploit this setup to study disorder-to-order transformation of Pt–Fe alloy nanoparticles, a material that is of great interest to fuel-cell electrocatalysis and ultra-high density information storage. In contrast to earlier reports, we show that Fe (instead of Pt) segregates towards the particle surface during annealing and forms a Fe-rich FeO_x outer shell over the alloy core. By combining both ex situ and in situ approaches to probe the interplay between ordering and surface-segregation phenomena, we illustrate that the surface segregation of Fe precedes the ordering process and affects the ordered phase evolution dramatically. We show that the ordering initiates preferably at the pre-existent Fe-rich shell than the particle core. While the material-specific findings from this study open interesting perspectives towards a controlled phase evolution of Pt–Fe nanoalloys, the characterization methodologies described are general and should prove useful to probing a wide-range of nanomaterials.

Fuel-cell research has witnessed tremendous progress in the recent past, forging a technology that in addition to holding pivotal scientific relevance, also enjoys a great industrial appreciation.[1–5] Catalysts design for the oxygen reduction reaction (ORR) in a proton-exchange membrane fuel cell (PEMFC), in particular, is an area that has received momentous thrust as an effect. The principal findings of this research effort provide much expansive insight into the fundamental understanding of nanoscale materials.[6–13] Although platinum (Pt) is known to exhibit exceptional activity towards the sluggish ORR kinetics, it still remains an economically nonviable option for large-scale implementation of PEMFC, owing to its depleting natural sources and exceedingly high costs.[5,6,14–16] Currently, there exists a clear agreement in the literature that nanoscale alloying of Pt with 3d transition metals (Pt–M alloys; M = Fe, Co, Ni, Cu), in addition to reducing the mass loading of Pt, also enhances catalytic activity towards the ORR.[5,16–24] Various bimetallic[18,25] and ternary alloy[26–29] systems have been investigated till date and the findings constantly suggest that ordered nanoalloys exhibit an extended catalytic durability over their disordered counterparts.[8,12,22,30–32]

Pt–Fe system, in particular, has gathered a lot of interest in recent years not only on the account of its enhanced ORR electrocatalysis,[8,12,20,22,28,33–36] but also because of its magnetic properties that are deployable in ultrahigh-density information storage.[10,37–42] The PtFe ($L1_0$) ordered phase exhibits a very high uniaxial magnetocrystalline anisotropy along the *c* direction of the crystal structure. The Pt_3Fe ($L1_2$) phase delivers an enhanced ORR activity from the compressively strained Pt overlayers that encapsulate ordered alloy cores. Therefore, the chemical synthesis of Pt–Fe alloy nanoparticles in these ordered phases has been extensively studied in the past years. For example, novel alloy structures such as intermetallic Pt–Fe/Pt core shells,[8] Pt–Fe–Cu ternary alloy nanoparticles,[12] monodisperse Ni/FePt core shells,[35] and face-centered tetragonal (fct) FePt nanoparticles[36] have been explored with reported ORR specific activities of 0.55 mA cm^{-2}, 0.75 mA cm^{-2}, 1.95 mA cm^{-2}, and 3.16 mA cm^{-2}, respectively. Unfortunately, the wet-chemical synthesis yields disordered nanoparticles in the face-centered cubic (fcc) A1 phase. Hence, the thermal annealing procedure (typically at 800 °C, 1 h) is generally performed to transform disordered A1 phase into $L1_0$ or $L1_2$ phases. It is widely reported that the thermal annealing also promotes a preferential surface segregation of Pt in addition

[a] S. Prabhudev, Dr. M. Bugnet, Dr. G. A. Botton
Department of Materials Science and Engineering
McMaster University
Hamilton—L8S 4L8 (Canada)
E-mail: gbotton@mcmaster.ca

[b] Dr. M. Bugnet, Dr. G. A. Botton
Canadian Center for Electron Microscopy
Hamilton—L8S 4M1 (Canada)

[c] Dr. G.-Z. Zhu
School of Materials Science and Engineering
Shanghai Jiao Tong University
Shanghai, 200240 (P.R. China)

[d] Dr. C. Bock
National Research Council Canada
Ottawa—K1A 0R6 (Canada)

Supporting information for this article is available on the WWW under http://dx.doi.org/10.1002/cctc.201500380.

© 2015 The Authors. Published by Wiley-VCH Verlag GmbH & Co. KGaA. This is an open access article under the terms of the Creative Commons Attribution-NonCommercial License, which permits use, distribution and reproduction in any medium, provided the original work is properly cited and is not used for commercial purposes.

AEM 3 This publication is part of a Special Issue on Advanced Microscopy and Spectroscopy for Catalysis. Once the full issue has been assembled, a link to its Table of Contents will appear here.

to the ordering process.[21,33,34,43–48] The preference of Pt over Fe is ascribed to the larger atomic radius and low surface energies of Pt atoms as compared to Fe. On the contrary, we report herein on the surface segregation of Fe. Using atomic-resolution imaging under scanning transmission electron microscopy (STEM) and electron energy loss spectroscopy (EELS), we show that the annealed Pt–Fe nanoparticles bear an Fe-rich shell over the alloy core. We find that the thermal annealing can result in unique structures including (i) Pt–Fe alloy (core)–Pt-rich (inner shell)–Fe-rich (outer shell), (ii) Pt-rich alloy (core)–Fe-rich (shell), and (iii) PtFe-$L1_0$ (core)–Fe-rich (shell), based on the core alloy composition. To get a better insight into the surface segregation of Fe and its order of occurrence with respect to atomic ordering, we also investigated the phase transformation of a single nanoparticle in situ, over the course of annealing. Our findings reveal that the surface segregation of Fe precedes the ordered transformation. Finally, we also illustrate a dramatic effect that the pre-existent Fe-rich shell can have on the atomic-ordering process.

Results and Discussion

Pt–Fe alloy nanoparticles were synthesized by impregnating Pt/C precursors with appropriate amounts of $Fe(NO_3)_3{\cdot}9H_2O$ salt (see Experimental Section for details). Subsequent annealing at 800 °C (1 h, 8% H_2/Ar atmosphere) resulted in structures shown in Figure 1. The images in Figure 1 a1 and 1 b1 are atomic-resolution STEM high-angle annular dark-field images (STEM–HAADF, see Experimental Section for details) of the particles characterized. In Figure 1 a1, the particle core architecture (viewed along [1 1 0] zone axis) exhibits alternating bright and dark intensities. STEM–HAADF is an atomic-number (Z) contrast technique with image intensities roughly proportional to $Z^{1.7}$. Hence, the alternating bright and dark intensities observed in Figure 1 a1 correspond to atomic columns of Pt and Fe, respectively. Thus, the images confirm that the particle transformed into an ordered alloy core architecture upon annealing. The particle in Figure 1 b1, however, is off a zone axis highlighting this alternating intensity and, therefore, the ordering is not obvious.

Further, the elemental distribution of Pt and Fe within these nanoparticles was examined using STEM–EELS compositional mapping (see Experimental Section for details) as shown in Figure 1 a2–a4 and Figure 1 b3–b5. Figure 1 a2, a3 reveal the projected Fe and Pt distribution within the particle shown in Figure 1 a1. The Pt-versus-Fe composite map (Figure 1 a4) indicates that the particle core is composed of Pt–Fe alloy. It is also visible from a detailed inspection of Figure 1 a4 that the core is surrounded by two shells, 1) surface-segregated Fe-rich outer shell and 2) Pt-rich inner shell. For better clarity, an EELS line profile (Figure 1 a5) was taken along the white arrow indicated in Figure 1 a4. From the Fe $L_{2,3}$-edge (green) and Pt $M_{4,5}$-edge (red) profiles between 1.0 and 2.05 nm in Figure 1 a5, the Fe-rich outer shell (≈0.7 nm thick) and Pt-rich inner shells (≈0.2 nm thick) are clearly evidenced. Additional confirmation can also be found in the EELS spectra (ranging from 600 eV to 2500 eV) provided in Figure 1 a6; the spectrum in blue and green corresponds to a region in the particle core (dotted blue box in Figure 1 a4) and Fe-rich shell (dotted green box in Figure 1 a4), respectively. In the blue spectrum (core region), both Fe $L_{2,3}$-edge (at 708 eV) and Pt $M_{4,5}$-edge (at 2206 eV) can be identified, confirming the Pt–Fe alloy core structure. However, in the green spectrum (outer shell region), only the Fe L-edge can be identified with no evidence of Pt. Notably, the surface-segregating Fe atoms in the nanoparticles could interact with the annealing atmosphere (reducing H_2/Ar atmosphere), and even traces of O_2 (ppm level) present in the reducing H_2–Ar mixture can cause oxidation.[49] This can be confirmed by analyzing the EELS spectrum (of the shell region) ranging between 450 eV and 900 eV, in which the O–K edge can be identified, as shown in Figure 1 a7. From Figure 1 a6 and 1 a7, it can therefore be confirmed that the outer shell is Fe-rich (FeO_x).

The micrographs in Figure 1 b3 and b4 reveal the projected Fe and Pt distribution within the particle described in Figure 1 b1. The Pt-versus-Fe composite map (Figure 1 b5) indicates that the Pt-rich alloy core is surrounded by a surface-segregated Fe-rich shell (≈0.35 nm thick). Unlike the particle shown in Figure 1 a4, there is no evidence of Pt segregation in this particle. For a better visibility of surface-segregated Fe-rich shell, a small region (dotted red lines) in the STEM–HAADF image (Figure 1 b1)) was bandpass-filtered to generate the picture in Figure 1 b2. This filtering is solely used to improve the visibility of the weaker intensities adjacent to the strongly scattering Pt atoms so that the dynamic range of the images allows visualizing the existing structure. The segregated Fe-rich shell (region outside the yellow line) surrounding the Pt-rich alloy core is clearly visible in the band-pass filtered image (Figure 1 b2).

From the results presented in Figure 1, it is clear that nanoparticles emerged with a surface-segregated Fe-rich shell upon thermal annealing (see Supporting Information, Figure S1, for additional statistics). However, this finding is in apparent contradiction to earlier reports that suggested a surface segregation of Pt.[33,34,43–48] In general, the segregation phenomenon of bimetallic systems is based on the surface energies and atomic radii of two metals, with the element having a larger atomic radius and a lower surface energy segregating towards the free surface.[43,50] However, kinetics can certainly play a dominant role over thermodynamics in nanoscale phase transformations. It appears that the segregation of Fe atoms is kinetically more favored over Pt to result in the formation of core (alloy)–shell (Fe-rich) structures described in Figure 1. Irrespective of the element segregating towards the surface, these studies clearly indicate that the thermal annealing procedure results in both ordering and surface-segregation events that can influence the other. Therefore, it is crucial to investigate their relative orders of occurrence. In the following, we illustrate that surface segregation of Fe precedes the ordering process, using both ex situ and in situ methods. The ex situ methodology involved comparing the nanoparticle structures annealed at 800 °C (Figure 1) with those annealed before the disorder-to-order phase-transition temperature (<500 °C). However, the ex situ analysis is vastly limited by the interferences derived from comparing nonidentical particles in the ensemble. There-

© 2015 The Authors. Published by Wiley-VCH Verlag GmbH & Co. KGaA, Weinheim

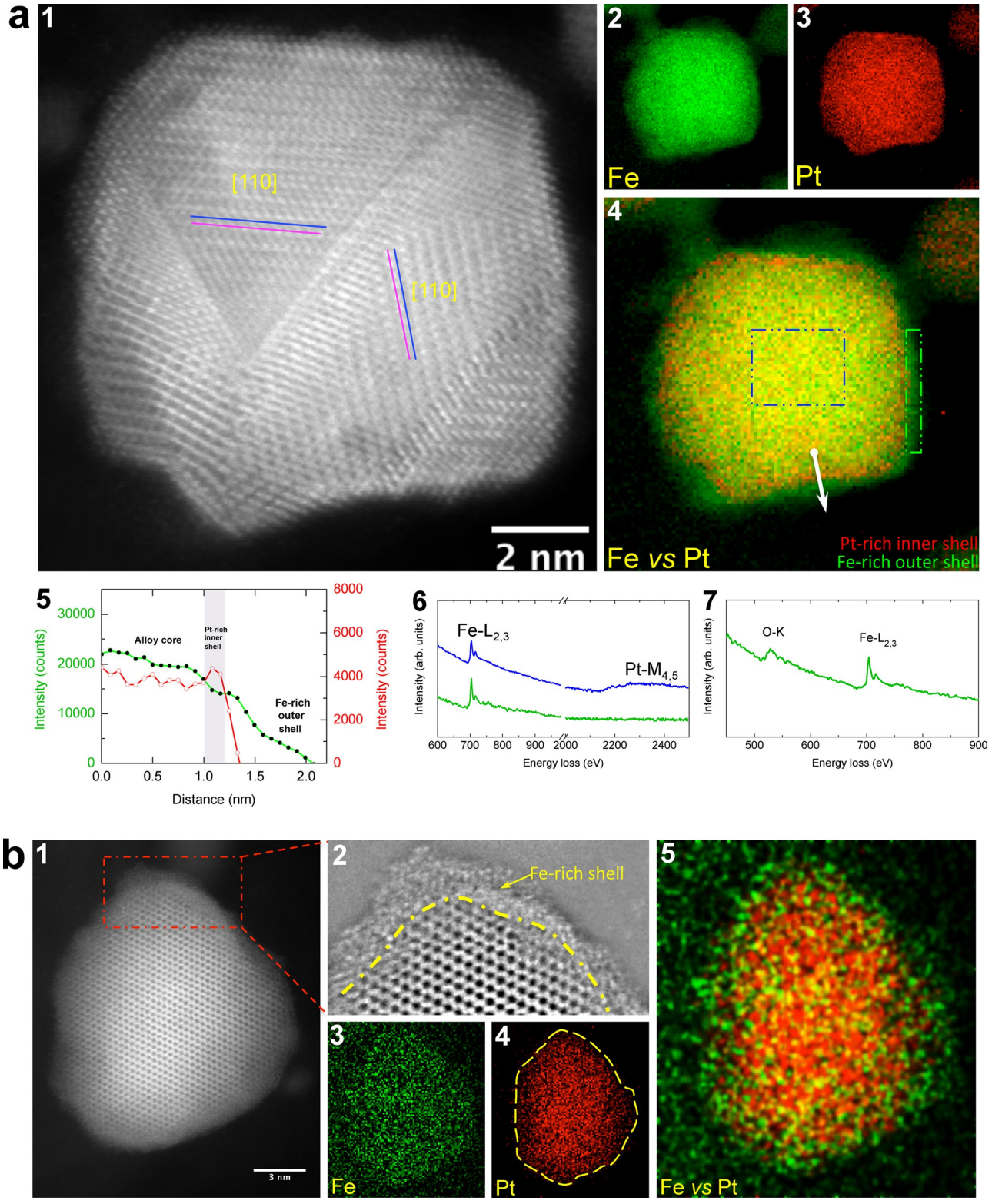

Figure 1. Atomic-resolution imaging and spectroscopy of Pt–Fe nanoparticles annealed at 800 °C (1 h). a, b) STEM–HAADF and STEM–EELS compositional maps of two different particles from the heat-treated sample. a1, b1) STEM–HAADF images. Parallel lines in a1 indicate alternating bright (pink) and dark (blue) intensities. The particle core in this region is close to [1 1 0] orientation. a2, b3) 2D EELS map of Fe (green). a3, b4) 2D EELS map of Pt (red). a4, b5) The composite Fe-versus-Pt maps. a5) EELS line profiles of Fe L-edge (green) and Pt M-edge (red) taken along the white arrow highlighted in a4. a6) EELS spectra (in the range 600 eV–2500 eV) integrated over a selected region at the core (dotted blue box) and the shell (dotted green box) in a4. a7) EELS spectra (in the range 450 eV–900 eV) integrated over the dotted green box region in a4. b2) Bandpass-filtered image of the region (marked in red) selected from b1.

© 2015 The Authors. Published by Wiley-VCH Verlag GmbH & Co. KGaA, Weinheim

fore, an in situ annealing experiment (up to 800 °C) was also performed by tracking the same nanoparticle over the course of heat treatment.

The results describing the ex situ method are discussed as follows. The STEM–HAADF images and STEM–EELS chemical maps shown in Figure 2 correspond to particles annealed at 300 °C (1 h, 8% H_2/Ar atmosphere). The annealing temperature was chosen based on the earlier work by Delalande et al, which showed that the disorder-to-order phase transition started at approximately 500 °C.[10] For better statistics, data from large areas covering a range of particle sizes were also collected (Figure 2a), alongside detailed analysis on one individual particle (Figure 2b). The STEM–HAADF image shown in Figure 2a(1) reveals dark patches (white arrows) within the particle core regions. The contrast in STEM–HAADF imaging is essentially sensitive to the atomic number and specimen thickness. Therefore, the observed dark patches in Figure 2a1 suggest compositional (Fe-rich regions) and/or structural inhomogeneity (voids) within the particle cores. The compositional inhomogeneity is better revealed from the STEM–EELS elemental profiles acquired at high spatial resolution. The EELS map in Figure 2b2 illustrates the projected Fe distribution within the particle shown in Figure 2b1. The white arrows marked in Figure 2b2 indicate the regions with depleted Fe content. The depletion in Fe over this region is compensated by an increase in Pt content, as confirmed by the corresponding Pt (red) versus Fe (green) composite map (white arrows in Figure 2b4), highlighting a compositional inhomogeneity within the particle core.

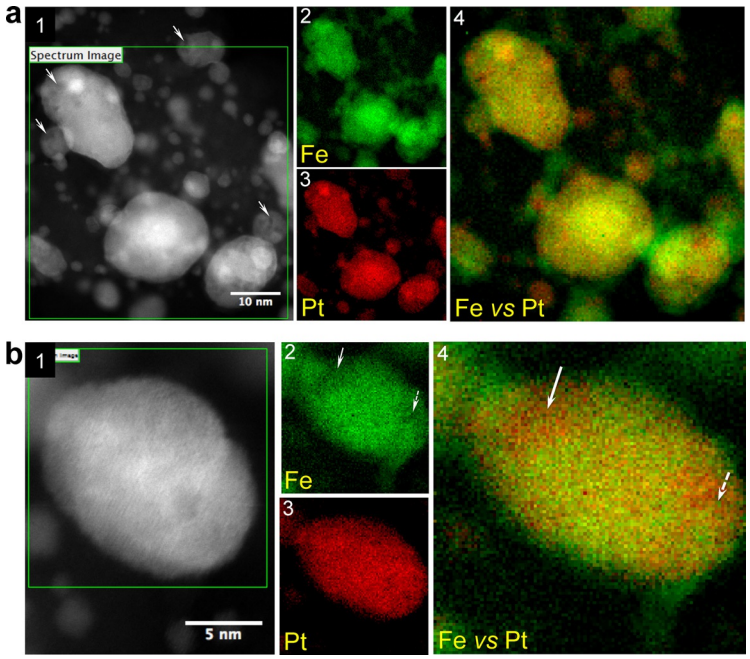

Figure 2. Elemental mapping of typical Pt–Fe nanoparticles annealed at 300 °C (1 h). a, b) STEM–HAADF and STEM–EELS compositional maps of two representative areas from the heat-treated sample. a1, b1) STEM–HAADF images. The white arrows in a1 indicate dark patches within the particle core, suggesting structural (voids) and/or compositional (Fe–rich) inhomogeneity. a2, b2) EELS maps of Fe. White arrows in b2 indicate regions with depleted Fe content. a3, b3) 2D EELS map of Pt. a4, b4) The composite Fe-versus-Pt maps. White arrows in b4 correspond to the Fe-depleted regions shown in b2 and indicate that the depleted Fe content is compensated with Pt, confirming compositional inhomogeneity within the particle core.

From the above findings, it is evident that the particle cores remain disordered (compositionally inhomogeneous) upon a thermal treatment at 300 °C. This is consistent with the predicted disorder-to-order phase-transition temperature (500 °C) by Delalande et al.[10] Furthermore, a careful observation of particle surfaces in the Pt (red) versus Fe (green) composite maps for both regions (Figure 2a4 and Figure 2b4) clearly indicate that the disordered particle cores are surrounded by Fe-rich shells. Therefore, from the ex situ methodology that involved comparing the nanoparticle structures annealed at 800 °C (Figure 1) with those annealed before the disorder-to-order phase-transition temperature (< 500 °C), it can be concluded that the surface segregation of Fe precedes the ordering process.

Importantly, the ex situ analyses involved comparing nonidentical particles. It can be argued that the local environments surrounding these particles were dissimilar and thereby, lead to varied segregation behaviors. These limitations can be overcome by tracking the same nanoparticle, over the course of annealing. In the following section, we illustrate this through an in situ annealing experiment. To the best of our knowledge, a simultaneous STEM–HAADF and STEM–EELS characterization on the same nanoparticle over the course of thermal treatment is unprecedented.

The in situ heating was performed inside an aberration-corrected STEM using a microelectromechanical systems (MEMS)-based heating holder (Aduro model from Protochips, see Experimental Section for details). The as-synthesized Pt–Fe nanoparticles were deposited onto the holder. Heat treatment involved an annealing procedure (under vacuum) by holding the sample at 200 °C, 400 °C, 500 °C, 600 °C, 700 °C, until 800 °C for 30 min each and finally quenching back to room temperature. At the onset, one as-synthesized particle was carefully picked from the ensemble. With the help of STEM–HAADF scans, the same nanoparticle was tracked over the course of thermal treatment. At every temperature, STEM–HAADF imaging coupled with STEM–EELS mapping was performed to obtain its structural and compositional information.

In Figure 3a and 3b, STEM–HAADF images of the as-synthesized Pt–Fe nanoparticles prior to heat treatment are shown. Similarly to Figure 2a1, the dark patches (yellow arrows) in these images confirm the disordered alloy structure. Further, to clarify that the as-synthesized particles did not already bear a Fe-rich shell, STEM–EELS elemental mapping was also performed on representative particles, and this is illustrated in the Supporting Information, Figure S2. Additionally, STEM–EDX analyses performed on randomly sampled particles (few tens in number) further confirm that the average composition of

© 2015 The Authors. Published by Wiley-VCH Verlag GmbH & Co. KGaA, Weinheim

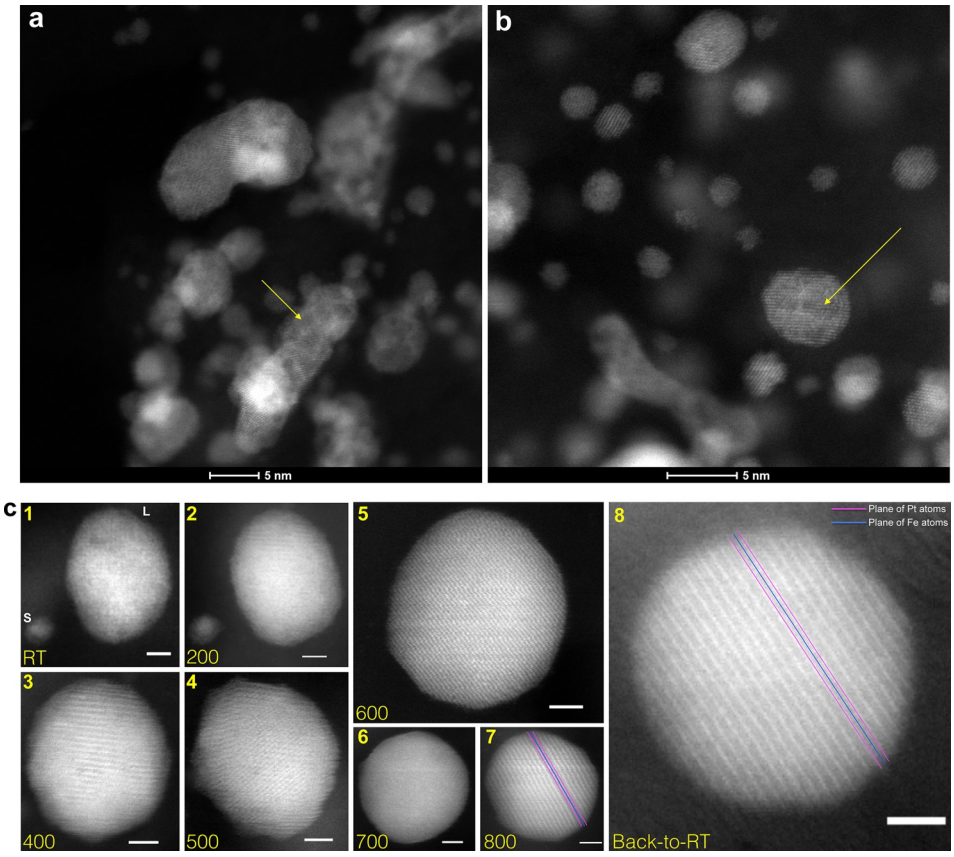

Figure 3. STEM–HAADF images of Pt–Fe nanoparticles at various stages of in situ thermal treatment. a, b) STEM–HAADF images of as-received Pt–Fe nanoparticles at room temperature. Yellow arrows indicate dark patches within the particle cores suggesting structural (voids) and/or compositional (Fe-rich) inhomogeneity. Scale bars 5 nm. c) STEM–HAADF images of particle L over the course of in situ thermal treatment. Scale bars 2 nm, RT = room temperature. c1) Initial particle L. c2–c7) Particle L at 200, 400, 500, 600, 700, 800 °C annealing temperature, respectively. c8) Particle L (0 0 1) planes parallel to electron beam) after quenching to RT. Parallel lines marked in pink and blue indicate alternating bright (Pt atomic-plane) and dark (Fe atomic-plane) intensities, respectively.

the as-prepared particles is approximately (67 ± 5)% Pt and (33 ± 5)% Fe. The STEM–HAADF image in Figure 3 c1 shows one such disordered particle (size = 9 nm) that was chosen for in situ tracking. For purposes of clarity, this large particle shall be identified as particle L in future discussions. The series of images shown in Figure 3 c2–c8 illustrate particle L tracked over various stage during annealing. Note that the STEM–HAADF images and STEM–EELS spectra were acquired after 30 min at every temperature. Hence, the labeled value of 400 in Figure 3 c3 for instance, indicates that the particle was exposed to 200 °C (for 30 min) plus 400 °C (for 30 min) overall. For better clarity, a schematic representation of the temperature profile is provided in Figure S3.

In Figure 4 a–d STEM-EELS compositional analyses of the particle L are shown at 400, 600, 700, and 800 °C, respectively. In addition to the typical elemental mapping (Figure 4 a1, 4 b1, 4 c1, 4 d1) as before, the line profiles of Fe L-edge (green) and Pt M-edge (red) were also extracted, along the blue (Figure 4 a2, 4 b2, 4 c2, 4 d2) and yellow (Figure 4 a3, 4 b3, 4 c3, 4 d3) scan directions.

In the Figure 4 a3, the Fe (green) and Pt (red) profiles reveal the presence of both Fe-rich (green arrow) and Pt-rich (red arrow) regions within the particle. The observed compositional inhomogeneity confirms that the particle L was still disordered at 400 °C. This is consistent with the fact that the overall heat transferred to particle from a treatment at 400 °C is lower than that from a treatment at the predicted disorder-to-order phase-transition temperature, i.e., 500 °C (Supporting Information, Section 1). Furthermore, the Fe (green) profile in Figure 4 a2 indicates that the particle surface is enriched in Fe (≈0.5 nm), as shown by the black arrows. Clearly, this must be the result of surface segregation of Fe as witnessed earlier from the ex situ approach (Figure 2). However, Fe enrichment at the surface is not seen in Figure 4 a3, based on a profile from the same particle, but taken in a different section, in which Pt-rich region (black arrows) can be seen exposed to the surface. Quantification of EELS intensities in these regions revealed a Pt/Fe content (on % basis) of 100.0/0.0 (black arrow on the left) and 75.4/24.6 (black arrow on the right). Hence, it can be concluded that although not complete enough to cover the surface entirely, the surface segregation of Fe began while the particle L still remained disordered. Consistent with the ex situ results discussed earlier, the in situ findings thus demonstrate that surface segregation of Fe precedes the ordering process during thermal treatment.

Additionally, a careful examination of the particle surface at 600, 700, and 800 °C (black arrows in Figure 4 b2, b3, c2, c3, d2, d3) reveals that the surface was fully covered with Fe-rich shell during later stages of annealing. As discussed below, our findings also reveal that the particle L finally existed in a PtFe-$L1_0$ (core)–Fe-rich (shell) alloy structure upon quenching to room temperature, following a disorder-to-order phase transition that occurred between the treatments at 400 °C and 800 °C. In Figure 5 a and 5 b, STEM–EELS mapping and line profiles are shown for the particle L at room temperature (upon quenching). Clearly, the particle core is surrounded by an Fe-rich shell (≈0.4 *nm* thick) as revealed by the Fe (green) profile in Figure 5 b (indicated by black arrows). After accounting for Fe content in the shell region, it is noticeable from Figure 5 b that the EELS intensities of Pt M-edge match very closely with those of Fe L-edge. The EELS intensities were also quantified by using the standard procedure[51] of comparing the cross-

© 2015 The Authors. Published by Wiley-VCH Verlag GmbH & Co. KGaA, Weinheim

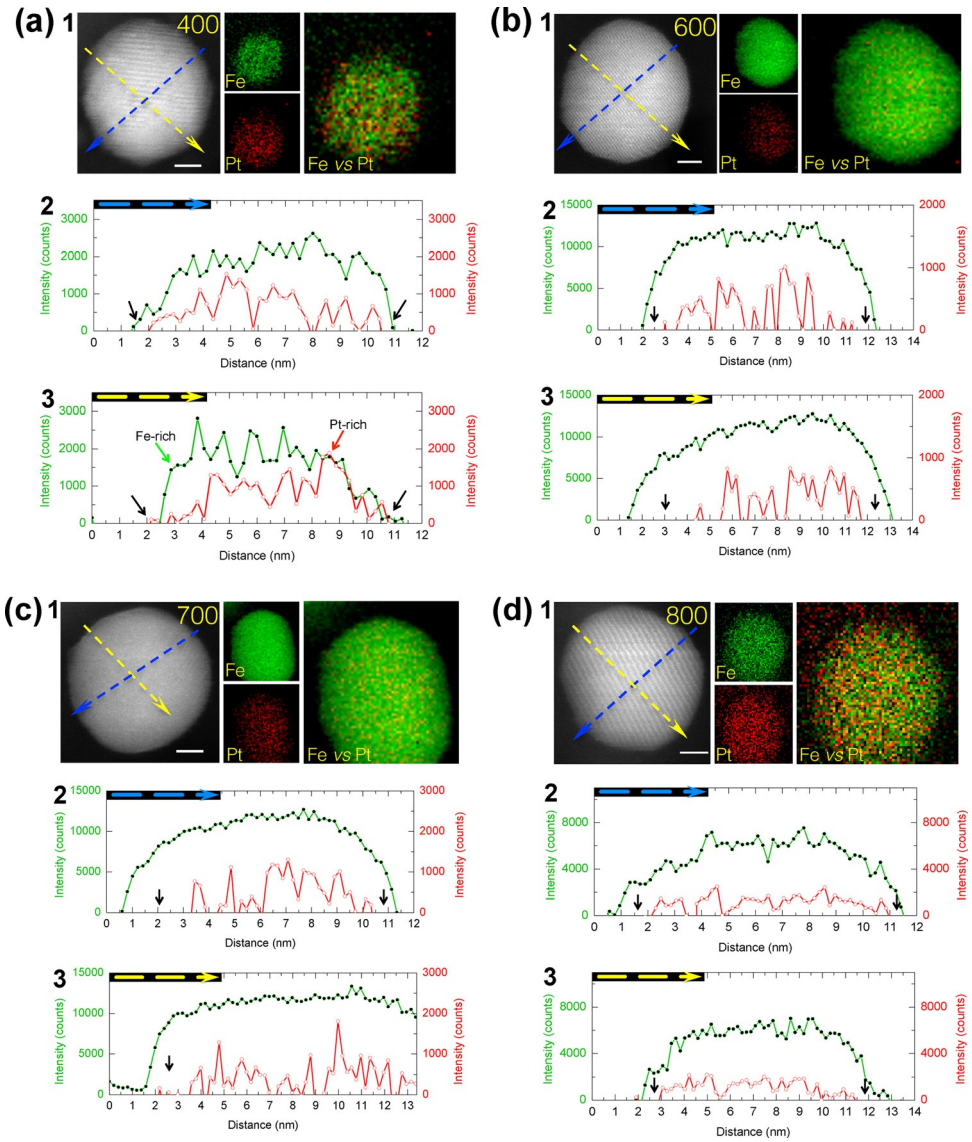

Figure 4. Elemental mapping and EELS line profiles across particle L at various stages of in situ thermal treatment. a–d) Data sets corresponding to 400, 600, 700, 800 °C, respectively. a1, b1, c1, d1) STEM–HAADF images plus 2D EELS maps of Fe (green), Pt (red), and the composite Fe versus Pt. Blue and Yellow arrows on the STEM–HAADF image indicate scan directions for EELS line profiles. Scale bars 2 nm. a2, b2, c2, d2) EELS line profiles of Fe L-edge (green) and Pt M-edge (red) taken along blue scan direction. a3, b3, c3, d3) EELS line profiles of Fe L-edge (green) and Pt M-edge (red) taken along yellow scan direction. For black arrows, see main text.

section weighted, background subtracted, integrated signals. In Table 1 the quantified Fe and Pt contents on overall particle (58.2% Fe, 41.8% Pt), core (56.7% Fe, 43.3% Pt), and the shell (93.7% Fe, 6.3% Pt) regions are listed. This suggests an approximately 50:50 compositional mixture of Pt and Fe in the particle core, which therefore should exist in $L1_0$ ordered phase as dictated by the phase diagram. The corresponding STEM–HAADF image shown in Figure 3c8 resolves the ambiguity, by revealing alternating bright and dark intensities within the particle (with (0 0 1) planes oriented parallel to electron beam) that, owing to atomic-number contrast, correspond to Pt and Fe atomic planes, respectively. The present observation that the particle L existed with an $L1_0$ ordered core alloy structure after the treatment and the earlier finding that the particle remained disordered at 400 °C suggest that the disorder-to-order phase transition in particle L occurred between the treatments at 400 and 800 °C. Notably, this inference is very well consistent with the predicted disorder-to-order phase transition (≈500 °C) by Delalande et al.[10]

Finally, in Figure 5c the EELS spectra (between 450 and 800 eV), recorded over an integrated area in the shell region, for the in situ and ex situ annealed particles are shown. For the ex situ annealed particle, as discussed earlier in Figure 1a7, evidence for the Fe-rich shell as FeO_x can be found by identifying O K and Fe $L_{2,3}$-edges. However, for the in situ annealing experiment it is expected that the vacuum maintained inside the microscope column contained significantly low concentration of O_2 compared to that under ex situ annealing atmosphere. Hence, the Fe-rich FeO_x shell is more likely to be pure Fe shell. This can be evidenced by the absence of O K-edge in the pink spectrum shown in Figure 5c that corresponds to the in situ annealed particle. These observations therefore suggest that the surface segregation of Fe occurred even under a minimum availability of O_2.

Other processes such as Ostwald ripening and coalescence were also captured during the in situ annealing experiment, and the details can be found in Figure S4. By acquiring a time series of STEM–HAADF images, we were able to capture (1) shrinking of a small particle (≈2.5 nm) through atom migration (Figure S4(a)), and (2) an atomic cluster (≈1 nm) detaching from an intermediate-size particle to coalesce with neighboring bigger particle (Figure S4(c)). Expectedly, these phenomena would enable a mass transport between the particles that might further lead to variations in the composition as well as particle size, over the course of thermal treatment.

So far, we have demonstrated surface segregation of Fe and its precedence over the ordering process using both ex situ and in situ approaches. We can surmise that the pre-existent Fe-rich shell can serve as a heterogeneous boundary to these single-crystal nanoparticles and, consequently, affect the order-

© 2015 The Authors. Published by Wiley-VCH Verlag GmbH & Co. KGaA, Weinheim

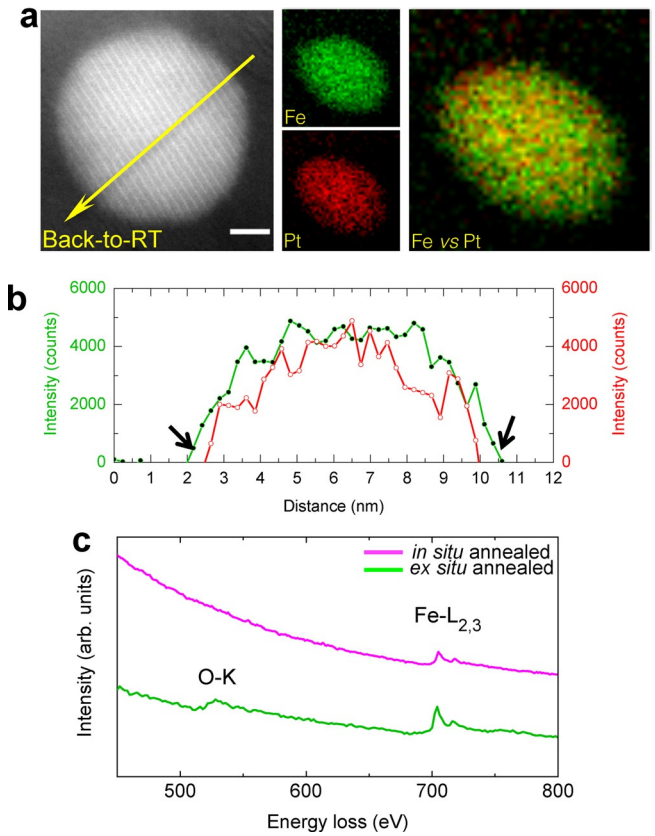

Figure 5. Elemental mapping and EELS line profiles across particle L after in situ thermal treatment. a) STEM–HAADF image plus 2D EELS maps of Fe (green), Pt (red), and the composite Fe versus Pt. These data were acquired after the heat-treated particle L was cooled down to room temperature (RT). The yellow arrow in the STEM–HAADF image indicates the direction for taking EELS line profiles. b) EELS line profiles of Fe L-edge (green) and Pt M-edge (red) taken along yellow direction. Black arrows indicate the presence of an Fe-rich shell (≈0.4 nm thick) at the particle surface. Black arrows, see main text. c) EELS spectra (in the range 450–800 eV) integrated over a selected region at the shell of an in situ (pink) and ex situ (green) annealed particle.

Table 1. Elemental quantification of in situ annealed particle using EELS.

Region selected from EELS Spectrum Image[a]	Composition [%] Fe	Pt
Overall Particle	58.2	41.8
Core	56.7	43.3
Shell	93.7	6.3

[a] See Figure S5 for details.

ing mechanism. In Figure 6 one such dramatic effect is illustrated. The STEM–HAADF image of a nanoparticle annealed at 600 °C (1 h, 8% H_2/Ar atmosphere) is shown in Figure 6a. The nanoparticle is viewed along [110] zone axis and alternating bright (pink) and dark (blue) intensities are highlighted in the regions identified by yellow arrows. As in Figure 1a1, these bright and dark fringes correspond to atomic columns of Pt and Fe, respectively. Clearly, their presence confirms the ordering process. However, these alternating bright and dark atomic planes can only be seen as pockets and not homogenously distributed throughout the particle. This observation suggests that the ordering process is still not complete. The dashed red box drawn in Figure 6a clearly identifies this transition, in which a progressive ordering front is evident on the left half (visible as alternating intensities), and the region onto right half shows no evidence of atomic ordering. The image in Figure 6b is a gamma-adjusted STEM–HAADF image corresponding to the image in Figure 6a and a close observation at the particle surface reveals the segregated Fe-rich shell as indicated. Noticeably, the atomic ordering starts at the Fe-rich shell and propagates inwards (yellow arrows). Similar observations can also be made on the small particle also visible in Figure 6a and b, such as the Fe-rich shell covering the particle surface and the initiation of the ordering process at the Fe-rich shell (Figure 6a, the color code for the arrows and lines can be found in the figure caption). This effect must be caused by the pre-existent Fe-rich shell that provides a heterogeneous boundary to the nanoparticle. Therefore, the formation of nuclei ($L1_0$ or $L1_2$) for ordering is expectedly more favored to initiate at the Fe-rich shell than the particle core. Notably, the local elemental distribution can also play a dominant role in the formation of these ordered nuclei. For instance, in the region identified by dashed yellow box in Figure 6a, a local enrichment in Pt concentration is evidenced, as revealed by the bright intensities of the atomic columns with a lattice spacing of 0.20 nm. Hence, despite the proximity of this region to the Fe-rich shell, ordering process is not initiated.

In addition, there are also interesting crystallographic effects that can be identified in these particles. Consider the region identified by solid yellow box (1) shown in Figure 6a. Along (001), the first atomic planes pointed at with short pink arrows show bright intensity, whereas the latter ones in the particle core alternate with bright (long pink line) and dark intensity (long blue lines). Similar observations can be made for the regions identified by solid yellow boxes (2) and (3), in which the bright intensity for the terminating atomic columns/planes are identified (short pink arrows). From the previous discussions, it is clear that the observed bright and dark intensity on a particle oriented in [110] correspond to atomic columns of Pt and Fe, respectively. Thereby, the identified terminating atomic planes/columns in boxes (1), (2), and (3) confirm segregation of Pt over the ordered particle core. However, notably, the segregated Pt atomic layer is still underneath the surface-segregated Fe-rich shell (Figure 6b).

Conclusions

Using atomic-resolution imaging and electron energy loss spectroscopy, we have demonstrated the surface segregation of Fe in annealed Pt–Fe alloy nanoparticles. This finding is in contrast with earlier reports that suggested a Pt surface segregation. For probing the interplay between segregation and atomic ordering, we have looked beyond traditional ex situ characterization. Both imaging and electron energy loss spectroscopy were performed on one single nanoparticle, in situ, over the course of thermal treatment. By combining both

© 2015 The Authors. Published by Wiley-VCH Verlag GmbH & Co. KGaA, Weinheim

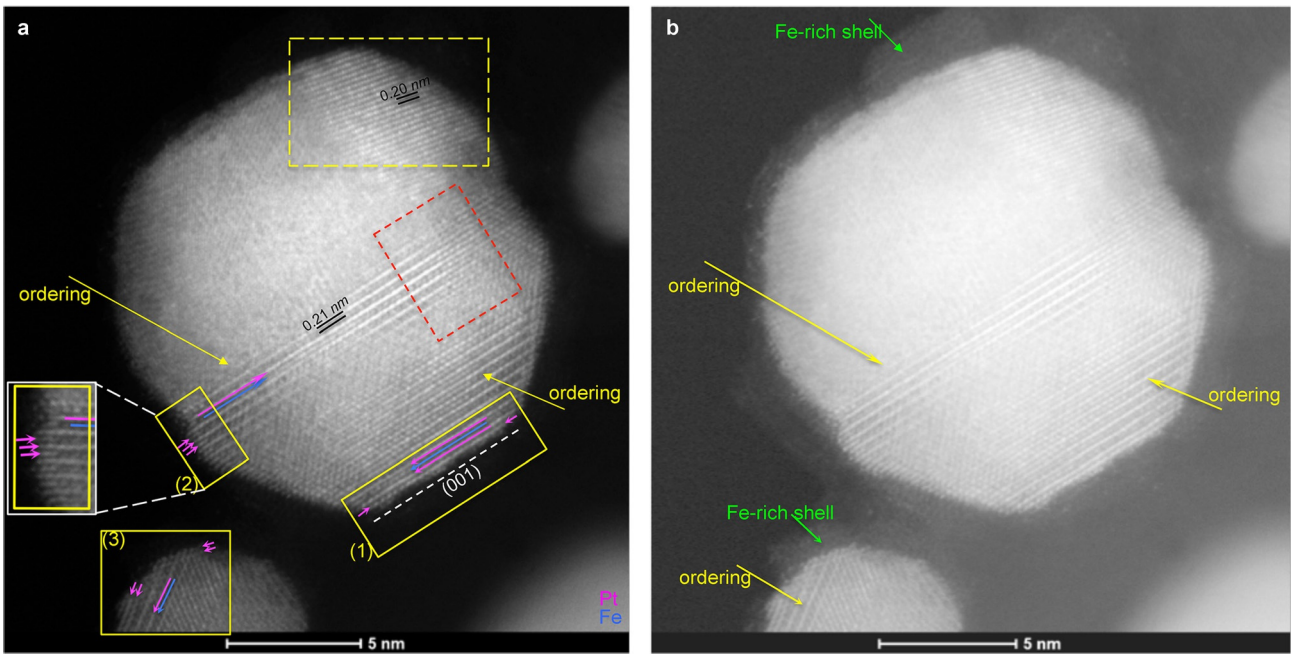

Figure 6. Atomic-resolution STEM–HAADF images of a Pt–Fe nanoparticle annealed at 600 °C (1 h). a) STEM–HAADF image of the particle viewed along [1 1 0] zone-axis. Parallel lines drawn in pink and blue indicate bright and dark intensities, respectively. Yellow arrows identify the regions where alternating bright and dark intensities can be observed. Solid yellow boxes (1, 2, 3) and enlargement of (2) identify regions with terminating atomic columns with bright intensities. The dashed red box identifies a transition region. The dashed yellow box identifies a region locally enriched in Pt. Explanations of pink and blue arrows are given in the main text. b) STEM–HAADF image generated after adjusting the gamma in (a). Green arrows indicate the Fe-rich FeO_x shell that could not be observed solely in (a). Yellow arrows indicate the ordering direction.

ex situ and in situ approaches, the segregation of Fe was shown to precede the ordering process. Various unique structures resulting from a typical thermal treatment were elucidated, including particles with (i) Pt–Fe alloy (core)–Pt-rich (inner shell)–Fe-rich (outer shell), (ii) Pt-rich alloy (core)–Fe-rich (shell), and (iii) PtFe-$L1_0$ (core)–Fe-rich (shell). The effect of such pre-existent Fe-rich shell on the ordering process was also studied and our findings reveal that the ordering is more favored to initiate at the Fe-rich shell than the particle core. This study opens interesting perspectives towards a rational design and a controlled phase evolution of Pt–Fe nanoalloys, ultimately intended for viable applications in ORR electrocatalysis and magnetic storage devices. Finally, the characterization methodologies described in this work is not limited to Pt-alloy nanoparticles, but should prove useful to an atomic-scale probing of a broad-range of nanostructures in general.

Outlook

Herein, we reported on the surface segregation of Fe during the thermal treatment of Pt–Fe alloy nanoparticles. Routinely, a vast majority of catalyst varieties, including the annealed Pt nanoalloy systems, undergo a pretreatment before the ORR measurements with a procedure termed voltammetric dealloying[52] (VD). The VD typically involves continuous electrochemical voltammetric sweeps between 0.05 and 1.2 V over 50–100 cycles. In addition, the charge resulting from the adsorption–desorption reaction of molecular H ($Q_{Hads/des}$) on Pt (between 0 and 0.3 V) is found to increase upon VD, indicating an increase in the electroactive Pt surface area (ECSA). Consequently, the resulting nanoparticle surfaces are reported to exhibit a surface catalytic activity that is approximately 5 times enhanced (Pt mass basis) compared to a nondealloyed catalyst particle.[52,53] Although a lot of research has been performed on correlating the observed increase in ECSA from VD with the effected modification to the nanoparticle surface-structures, the current knowledge is still vastly limited to interpreting the features in the recorded voltammograms with the aid of DFT calculations. Particularly, in the voltage range from 0.3 V to 0.7 V, a small oxidation peak is consistently observed during the first few VD cycles, and is seen to gradually diminish with the cycling number. With additional insights from DFT calculations,[54] these oxidation peaks have been attributed to the dissolution of Fe,[12] Cu,[52] Co,[31] and Ni[53] for Pt–M (M = Fe, Cu, Co, Ni) systems, and it is believed that the VD imparts a Pt skin structure by (1) dissolving these less noble metal alloy components from the surface and (2) promoting atomic rearrangement through surface-diffusion. For the Pt–Fe system, our present findings on the surface segregation of Fe in the annealed particles corroborate with the electrochemical viewpoint, validating that the origin of oxidation peaks observed during VD must be an effect of the surface dealloying of Fe-rich shell. For disordered Pt–M alloy nanoparticles, the VD has been shown to massively remove the less noble alloy component, associated with a drastic rearrangement of Pt surface atoms and bulk atoms by surface diffusion.[53] However, for the particles observed in this work, for which a Pt inner shell also exists underneath the Fe-rich shell, it still remains a question whether or not the VD in-

© 2015 The Authors. Published by Wiley-VCH Verlag GmbH & Co. KGaA, Weinheim

volves surface atomic rearrangement or serves merely as a surface-cleaning procedure. This crucial question needs to be addressed. Recently, we have performed an in situ potential cycling of disordered Pt–Fe nanoparticles inside a TEM.[55] In the future, by coupling this setup with the EELS technique, we look forward to gaining more insights into the surface tunability of the VD procedure.

Experimental Section

Nanoparticle synthesis

20 wt% Pt/C precursor powder was first made by using a method described in the literature[56] (briefly discussed as follows). The Pt/C precursor nanoparticles were made by depositing a specific volume of a colloidal Pt solution onto Vulcan XC-72R. The Pt colloids were synthesized by first dissolving $PtCl_4$ (0.4652 g, Alfa Aesar, 99.9% metal basis) in ethylene glycol (50 mL, EM Science) containing 0.15 M NaOH. The pH of the synthesis solution was known to define the resulting particle size of the Pt colloids. The solution was stirred for 1 h at RT, and subsequently heated under reflux at 160 °C for 3 h. A dark brown colloidal Pt solution was formed in this manner, which was then allowed to cool in air and at RT for 1 h, before mixing with Vulcan XC-72R (1.077 g) in a beaker, and finally was allowed to stir for 24 h. An appropriate amount of 1 M HNO_3 was added to adjust the pH to 2 allowing for complete deposition of the Pt colloids onto the carbon support. After 24 h, the Pt/C powder was filtered and extensively washed with water and ethanol. A clear filtrate was obtained indicating that the Pt colloids were completely deposited onto the carbon support. The powder was then dried in an air oven at 80 °C overnight, and subsequently homogenized in a glass mortar by grinding.

The as-synthesized Pt–Fe alloy nanoparticles were prepared by ultrasonically dispersing 500 mg samples of the Pt/C precursor powder (prepared with methods discussed above) in water (120 mL) in a 250 mL beaker for 1.5 h. $Fe(NO_3)_3{\cdot}9H_2O$ (Alfa Aesar, 99.99% Fe basis) was used as precursor salts. This precursor salt ($\approx$0.2072 g) was impregnated onto 20 wt% Pt/C suspension (0.5 g). Upon dissolution of the precursor salts, the pH of the suspension was adjusted to 4 by adding a few drops of 1 M HNO_3 to facilitate dissolution much further. The solution was then well stirred for 30 min at RT. Subsequently, the water was evaporated at a slow rate (for 3–4 h) and under stirring at 80 °C and the dried powders were then ground in a glass mortar to homogenize. These powders were then immersed in 1 M HNO_3 acid solution for 1 h under continuous magnetic stirring to leach out any single-phase Fe particles.

Scanning transmission electron microscopy (STEM)

Detailed structural characterization was performed using a FEI-Titan 80-300 cubed TEM, operated at 300 kV in scanning TEM mode (STEM). The microscope was equipped with a high-brightness Schottky electron source, aberration correctors for both probe-forming and image-forming lenses, a monochromator and a high resolution Gatan-Quantum spectrometer (Gatan Inc., Pleasanton, CA).

STEM–HAADF: Atomically resolved HAADF images were acquired in the STEM mode. At the operating conditions, a sub-angstrom resolution was achievable. Also called STEM–HAADF technique, these images are generated by collecting electrons scattered at high angles on passing through the samples, using a Fischione HAADF detector. The acquired image intensity is roughly proportional to $Z^{1.7}$, with Z is the atomic number of scattering atoms.

STEM–EELS: EELS reflects the inelastic process during the interaction between the incident electron beam with the sample[57] measured using a sophisticated spectrometer. As an added advantage, the raster scanning STEM probe can also be used for obtaining spatial information, by collecting the scattered electrons with annular dark field (ADF) detector. This combination of STEM–ADF imaging with the EELS is collectively termed as STEM–EELS. For this work, the STEM–EELS was performed in the FEI-Titan 80–300 cubed TEM, operated at 300 kV in STEM mode. EELS spectra were recorded with a Quantum-Gatan post-column Imaging Filter (GIF) to determine the Pt and Fe elemental distributions by analyzing Pt $M_{4,5}$ and Fe $L_{2,3}$ edges. The convergence semi-angle of the scanning probe was approximately 20 mrad and the collection semiangle for EEL spectra was approximately 40 mrad. Chemical maps were constructed by analyzing Pt $M_{4,5}$ and Fe $L_{2,3}$-edges using a power-law background subtraction. For the line profiles, respective Pt M-edge and Fe L-edge spectra were collected along 10–20 points across the nanoparticle.

Heating stage: Nanoparticles were heated in situ by using the Aduro heating system. The design involved a thermal e-chip attached to a dedicated heating holder manufactured by Protochips Inc., Raleigh, NC. The entire assembly provided a precise temperature control over 1200 °C with super fast heating rates up to 1000 °C per millisecond.

Acknowledgements

S.P, M.B, G-Z.Z and G.A.B are grateful to APC (CaRPE-FC grant) and NSERC (Discovery and Strategic grants) for supporting this work. The microscopy was carried out at the Canadian Centre for Electron Microscopy (CCEM), a national facility supported by NSERC and McMaster University. C.B acknowledges financial support provided by NRC.

Author Contributions: *S.P and G.A.B conceived and designed the experiments. C.B synthesized the nanoparticles and carried out ex situ heat treatments. S.P, M.B, and G-Z.Z jointly performed the in situ annealing experiment. Data analysis and processing were carried out by S.P and M.B. S.P drafted the manuscript with feedback from all the authors on results and revisions of the manuscript.*

Keywords: alloy nanoparticles · in situ electron microscopy · iron · phase transition · platinum

[1] J. Tollefson, *Nature* **2010**, *464*, 1262 – 1264.
[2] K. Kendall, *Nat. Mater.* **2002**, *1*, 211 – 212.
[3] B. C. Steele, A. Heinzel, *Nature* **2001**, *414*, 345 – 352.
[4] A. S. Aricò, P. Bruce, B. Scrosati, J. M. Tarascon, W. VanSchalkwijk, *Nat. Mater.* **2005**, *4*, 366 – 377.
[5] M. K. Debe, *Nature* **2012**, *486*, 43 – 51.
[6] R. Borup, et al., *Chem. Rev.* **2007**, *107*, 3904 – 3951.
[7] B. Patrick, H. C. Ham, Y. Shao-Horn, L. F. Allard, G. S. Hwang, P. J. Ferreira, *Chem. Mater.* **2013**, *25*, 530 – 535.
[8] S. Prabhudev, M. Bugnet, C. Bock, G. A. Botton, *ACS Nano* **2013**, *7*, 6103 – 6110.
[9] X. Tuaev, S. Rudi, V. Petkov, A. Hoell, P. Strasser, *ACS Nano* **2013**, *7*, 5666 – 5674.

 © 2015 The Authors. Published by Wiley-VCH Verlag GmbH & Co. KGaA, Weinheim

[10] M. Delalande, M. J.-F. Guinel, L. F. Allard, A. Delattre, R. Le Bris, Y. Samson, P. Bayle-Guillemaud, P. Reiss, *J. Phys. Chem. C* **2012**, *116*, 6866 – 6872.
[11] V. R. Stamenkovic, B. Fowler, B. S. Mun, G. Wang, P. N. Ross, C. A. Lucas, N. M. Marković, *Science* **2007**, *315*, 493 – 497.
[12] L. Chen, C. Bock, P. Mercier, B. MacDougall, *Electrochim. Acta* **2012**, *77*, 212 – 224.
[13] M. A. Asoro, D. Kovar, Y. Shao-Horn, L. F. Allard, P. J. Ferreira, *Nanotechnology* **2010**, *21*, 025701.
[14] N. Yousfi-Steiner, P. Mocoteguy, D. Candusso, D. Hissel, *J. Power Sources* **2009**, *194*, 130 – 145.
[15] E. F. Holby, W. Sheng, Y. Shao-Horn, D. Morgan, *Energy Environ. Sci.* **2009**, *2*, 865.
[16] H. A. Gasteiger, S. S. Kocha, B. Sompalli, F. T. Wagner, *Appl. Catal. B* **2005**, *56*, 9 – 35.
[17] J. Greeley, I. E. L. Stephens, a. S. Bondarenko, T. P. Johansson, H. a. Hansen, T. F. Jaramillo, J. Rossmeisl, I. Chorkendorff, J. K. Nørskov, *Nat. Chem.* **2009**, *1*, 552 – 556.
[18] W. Yu, M. D. Porosoff, J. G. Chen, *Chem. Rev.* **2012**, *112*, 5780 – 5817.
[19] A. Chen, P. Holt-Hindle, *Chem. Rev.* **2010**, *110*, 3767 – 3804.
[20] M. C. Y. Chan, L. Chen, F. Nan, J. F. Britten, C. Bock, G. a. Botton, *Nanoscale* **2012**, *4*, 7273 – 7279.
[21] S. Chen, W. Sheng, N. Yabuuchi, P. J. Ferreira, L. F. Allard, Y. Shao-Horn, *J. Phys. Chem. C* **2009**, *113*, 1109 – 1125.
[22] L. Chen, M. C. Y. Chan, F. Nan, C. Bock, G. A. Botton, P. H. J. Mercier, B. R. Mac-Dougall, *ChemCatChem* **2013**, *5*, 1449 – 1460.
[23] C. Chen, et al., *Science* **2014**, *343*, 1339 – 1343.
[24] C. Cui, L. Gan, M. Heggen, S. Rudi, P. Strasser, *Nat. Mater.* **2013**, *12*, 765 – 771.
[25] M. Cao, D. Wu, R. Cao, *ChemCatChem* **2014**, *6*, 26 – 45.
[26] B. N. Wanjala, B. Fang, S. Shan, V. Petkov, P. Zhu, R. Loukrakpam, Y. Chen, J. Luo, J. Yin, L. Yang, M. Shao, C.-J. Zhong, *Chem. Mater.* **2012**, *24*, 4283 – 4293.
[27] C. Wang, D. Li, M. Chi, J. Pearson, R. B. Rankin, J. Greeley, Z. Duan, G. Wang, D. Van der Vliet, K. L. More, N. M. Markovic, V. R. Stamenkovic, *J. Phys. Chem. Lett.* **2012**, *3*, 1668 – 1673.
[28] M. Ammam, E. B. Easton, *J. Power Sources* **2013**, *236*, 311 – 320.
[29] C.-L. Sun, Y.-K. Hsu, Y.-G. Lin, K.-H. Chen, C. Bock, B. MacDougall, X. Wu, L.-C. Chen, *J. Electrochem. Soc.* **2009**, *156*, B1249.
[30] L. Xiong, A. Manthiram, *J. Electrochem. Soc.* **2005**, *152*, A697.
[31] D. Wang, H. L. Xin, R. Hovden, H. Wang, Y. Yu, D. A. Muller, F. J. DiSalvo, H. D. Abruna, *Nat. Mater.* **2013**, *12*, 81 – 87.
[32] M. Vasiliev, *J. Phys. D* **1997**, *30*, 3037 – 3070.
[33] A. C. Johnston-Peck, D. A. Cullen, J. B. Tracy, *Part. Part. Syst. Charact.* **2013**, *30*, 678 – 682.
[34] V. R. Stamenkovic, B. S. Mun, M. Arenz, K. J. Mayrhofer, C. A. Lucas, G. Wang, P. N. Ross, N. M. Markovic, *Nat. Mater.* **2007**, *6*, 241 – 247.
[35] S. Zhang, Y. Z. Hao, D. Su, V. V. T. Doan-Nguyen, Y. T. Wu, Ji. Li, S. H. Sun, C. B. Murray, *J. Am. Chem. Soc.* **2014**, *136*, 15921 – 15924.
[36] Q. Li, L. Wu, G. Wu, D. Su, H. Lv, S. Zhang, W. Zhu, A. Casimir, H. Zhu, A. Mendoza-Garcia, S. Sun, *Nano Lett.* **2015**, *15*, 2468 – 2473.
[37] K. Sato, *Nat. Mater.* **2009**, *8*, 924 – 925.
[38] A. Kovács, K. Sato, V. Lazarov, P. Galindo, T. Konno, Y. Hirotsu, *Phys. Rev. Lett.* **2009**, *103*, 1 – 4.
[39] J. Wittig, J. Bentley, L. Allard, M. Wellons, C. Lukehart, *Microsc. Microanal.* **2008**, *14*, 216 – 217.
[40] C. Liu, T. J. Klemmer, N. Shukla, X. Wu, D. Weller, M. Tanase, D. Laughlin, *J. Magn. Magn. Mater.* **2003**, *266*, 96 – 101.
[41] M. Müller, P. Erhart, K. Albe, *Phys. Rev. B* **2007**, *76*, 155412.
[42] H. Chen, Y. Yu, H. L. Xin, K. A. Newton, M. E. Holtz, D. Wang, D. A. Muller, H. D. Abruña, F. J. DiSalvo, *Chem. Mater.* **2013**, *25*, 1436 – 1442.
[43] A. V. Ruban, H. L. Skriver, J. K. Norskov, *Phys. Rev. B* **1999**, *59*, 15990 – 16000.
[44] V. Stamenkovic, T. J. Schmidt, P. N. Ross, N. M. Markovic, *J. Phys. Chem. B* **2002**, *106*, 11970 – 11980.
[45] M. Müller, K. Albe, *Phys. Rev. B* **2005**, *72*, 094203.
[46] B. Yang, M. Asta, O. N. Mryasov, T. J. Klemmer, R. W. Chantrell, *Acta Mater.* **2006**, *54*, 4201 – 4211.
[47] K. L. Torres, G. B. Thompson, *Ultramicroscopy* **2009**, *109*, 606 – 611.
[48] L. Y. Han, U. Wiedwald, B. Kuerbanjiang, P. Ziemann, *Nanotechnology* **2009**, *20*, 285706.
[49] M. Ahmadi, F. Behafarid, C. Cui, P. Strasser, B. R. Cuenya, *ACS Nano* **2013**, *7*, 9195 – 9204.
[50] C. Cui, M. Ahmadi, F. Behafarid, L. Gan, M. Neumann, M. Heggen, B. R. Cuenya, P. Strasser, *Faraday Discuss.* **2013**, *162*, 91 – 112.
[51] J. Verbeeck, S. Van Aert, *Ultramicroscopy* **2004**, *101*, 207 – 224.
[52] P. Strasser, S. Koh, C. Yu, *ECS Trans.* **2007**, *11*, 167 – 180.
[53] P. Mani, R. Srivastava, P. Strasser, *J. Power Sources* **2011**, *196*, 666 – 673.
[54] P. Strasser, S. Koh, J. Greeley, *Phys. Chem. Chem. Phys.* **2008**, *10*, 3670 – 3683.
[55] G. Z. Zhu, S. Prabhudev, J. Yang, C. M. Gabardo, G. A. Botton, L. Soleymani, *J. Phys. Chem. C* **2014**, *118*, 22111 – 22119.
[56] C. Bock, C. Paquet, M. Couillard, G. A. Botton, B. R. MacDougall, *J. Am. Chem. Soc.* **2004**, *126*, 8028 – 8037.
[57] G. A. Botton, *Sci. Microsc.* **2007**, 273 – 405.

Received: April 25, 2015
Revised: July 6, 2015
Published online on October 1, 2015

 © 2015 The Authors. Published by Wiley-VCH Verlag GmbH & Co. KGaA, Weinheim